Current Science
CS 5 (3), 2227-2253 (2025)
Received 13 Feb 2025 | **Revised 15 March** 2025 | **Accepted 13 April**. 2025 | **Online Available 10 May** 2025
https://doi.org/ 10.52845/CS/2025-5-3-15

Current Science

Current Science

OPEN ACCESS

ISSN (O) 2795-8639

Original Article

Comparative Investigation of Cavitation Performance by using Integrated Induced Impeller for the High-Speed Centrifugal Pump

Xingyu Fang[a,b], Tengjiao Guo[a,b], Ran Tao[a,b], Yanzhao Wu[a,b], Ruofu Xiao[a,b,*], Kun Lin[c,*]

[a]**College of Water Resources and Civil Engineering, China Agricultural University, Beijing 100083, China**

[b]**Beijing Engineering Research Center of Safety and Energy Saving Technology for Water Supply Network System, China Agricultural University, Beijing 100083, China**

[c]**Dongfang Electric Machinery Co. Ltd., Deyang 618000, China**

[*]**Corresponding Author: Ruofu Xiao**

Abstract:
To investigate and compare the external characteristics and cavitation resistance performance of the integrated induced impeller and the inducer-impeller, this paper takes the integrated induced impeller and the inducer-impeller of a certain high-speed centrifugal pump as the research subjects. Based on a combination of experiments and CFD numerical simulations, it is found that the external characteristics of the integrated impeller are inferior to those of the inducer-impeller. On the basis of quantitative and qualitative analysis, the internal cavitation flow of the integrated induced impeller and the inducer-impeller is carefully analyzed, from the initial cavitation state to the critical cavitation state and then to the large-scale cavitation inside the impeller. The critical cavitation number σ of the integrated induced impeller is much smaller than that of the inducer-impeller, σ =0.101 compared to σ =0.338. Subsequently, the blade is expanded at a span of 0.9, linking the cavitation on the blade with the load distribution on the blade, it is concluded that the cavitation resistance performance of the integrated induced impeller is significantly better than that of the inducer-impeller.

Keywords: Integrated induced impeller; Cavitation; High-Speed centrifugal pump

Introduction

Cavitation has always been a hot and difficult issue in the research of high-speed pumps. Cavitation refers to the process of forming vapor bubbles in the low-pressure areas of the liquid flow field. Essentially, it is a two-phase turbulence of gas and liquid, involving complex momentum transfer and energy exchange between the two. It can severely damage the structure of fluid machinery and affect the steady performance of fluid machinery [1], Additionally, cavitation also affects the unsteady characteristics of the flow [2-5]. Pumps have a very wide range of applications in production and life in water conservancy, agriculture, chemical industry and other fields. Wherever there is fluid flow, there is the operation of pumps. High-speed centrifugal pumps, characterized by small flow rate, high head, and compact structure, are widely used in industries such as aviation and shipbuilding [6]. However, due to factors such as high rotation speed and harsh operating environments, high-speed centrifugal pumps are extremely prone to cavitation.

Cavitation types can be divided into Traveling cavitation, Attached cavitation, Vortex cavitation, and Cloud cavitation [7]. Tan [8] analyzed the unsteady flow within the volute of a centrifugal pump under non-cavitating and cavitating conditions and found that in severe cavitation cases, the maximum value of pressure pulsations inside the volute is twice that under non-cavitating conditions. Athavale [9] used the Singhal

cavitation model to simulate cavitating vortex flows in axial flow pumps, centrifugal pumps, and turbine pumps, and found that cavitation occurred at the leading edge of the blades in all three types of pumps. Li et al. [10] analyzed the changes in the cavitation area on the surface of the impeller of a centrifugal pump under different cavitation number conditions and found that as the cavitation number gradually decreases, the size of the cavitation area significantly increases, which in turn leads to a downward trend in the overall performance of the centrifugal pump. Lu et al. [11] conducted numerical simulations and experimental studies, finding that compared to the outlet, the pressure pulsations at the inlet of the centrifugal pump have a greater correlation with cavitation. Cavitation generated by fluid flow is a complex two-phase turbulence, where vortex structures in the flow field can intensify the intensity and complexity of turbulence. Cavitation not only affects the performance decline of centrifugal pumps but also causes structural vibrations, leading to noise generation in centrifugal pumps [12-14].

Improving the cavitation performance of pumps and reducing the scale of cavitation development within the pump has always been a hot topic, Direct interference, indirect influence, and cavitation-site redesign are the three main methods of improvement. Zhu et al. [15] optimized the leading edge of the mixed-flow pump impeller, which improved the cavitation performance of the mixed-flow pump, providing a reference for optimizing the cavitation performance of impeller pumps. Yang et al. [16] conducted research on the splitter blades in a double-suction centrifugal pump and found that the pressure sharing between the long blades and the splitter blades is beneficial for improving the pump's cavitation performance. Zhang et al. [17] used genetic algorithms and decision trees to optimize the shape of the leading edge of centrifugal pump impeller blades, effectively improving the cavitation performance of the centrifugal pump. Adding an inducer at the front end of the centrifugal pump impeller can improve the cavitation performance of the centrifugal pump, Pouffary et al. [18] believes that numerical simulation provides useful assistance for the design of inducers in centrifugal pumps. Scholars have conducted research on the cavitation resistance performance of high-speed centrifugal pumps and found that compared to the inducer, the impeller region exhibits a more pronounced asymmetric cavitation phenomenon, and the pump's cavitation resistance performance worsens with increasing rotational speed [19-20]. Zhang et al. [21] conducted research on the cavitation performance of high-speed inducers under conditions of large flow rates and found that the cavitation performance of the three-blade inducer is superior to that of the two-blade inducer. Ma et al. [22] studied the cavitation performance of constant pitch and variable pitch inducers and found that the constant pitch inducer has better resistance to initial cavitation, while the variable pitch inducer has better ability to suppress the development of cavitation. The addition of splitter blades can increase the head and efficiency of the centrifugal pump [23]. Kergourlay et al. [24] introduced splitter blades in the design of the hydraulic centrifugal pump impeller, making the flow velocity and pressure distribution more balanced at the periphery of the impeller. Chabannes et al. [25] conducted research on the splitter blades in pumps with extremely low specific speeds and believes that increasing the number of splitter blades inside the pump is beneficial. Korkmaz et al. [26] conducted research on the splitter blades in deep well pumps and found that adding splitter blades amounting to 85% of the pump's blade area resulted in the highest efficiency for the deep well pump. Scholars have conducted research on the impact of splitter blades on the performance of centrifugal pumps and found that splitter blades can reduce pressure pulsations within the pump, thereby improving the pump's performance [27-28].

This article compares the external characteristics of the integrated induced impeller with those of the inducer-impeller and further analyzes the cavitation characteristics of both types of impellers. The comparative analysis of the two impellers illustrates the advantages of the integrated induced impeller, providing a reference for impeller selection in engineering applications.

1. Mathematical Methods

1.1. Governing Equations

Governing equations serve as the theoretical foundation and starting point for solving flow analysis problems. It is generally considered that

the fluid inside fluid machinery is incompressible, hence its internal flow can be described by the continuity equation and the momentum equation, namely, the Navier-Stokes equations.

Continuity Equation:

$$\frac{\partial u_i}{\partial x_i} = 0 \qquad (1)$$

Momentum equation:

$$\frac{\partial(\rho u_i)}{\partial t} + \frac{\partial(\rho u_i u_j)}{\partial x_j} = \frac{\partial}{\partial x_j}(\mu \frac{\partial u_i}{\partial x_j}) - \frac{\partial p}{\partial x_i} + \rho f_i \qquad (2)$$

In the equation, ρ is the fluid density, u_i (i =1,2,3) are the velocity components of the fluid, t is time, μ is the dynamic viscosity of the fluid, p is the pressure, and f_i are the components of the body force.

1.2.Turbulence Model

The SST k-ω model overcomes the deficiencies of the standard k-ω and BSL k-ω models by introducing the effects of shear stress transport into the turbulent eddy viscosity, offering highly accurate predictions for the onset and quantity of flow separation under adverse pressure gradients, and providing greater precision for boundary layer flow simulations. These superior performance characteristics have been proven by a multitude of fundamental research studies. For free shear flows, the SST model is equivalent to the k-ε model.

The standard k-ω model is based on Wilcox's k-ω formulation, which is characterized by its treatment of near-wall flows at low Reynolds numbers, enabling a smooth transition from the low-Reynolds-number form to the wall function. This model lacks complex nonlinear damping functions and is considered more accurate and robust compared to the k-ε model.

The standard k-ω model assumes that the turbulent viscosity is related to the turbulent kinetic energy and the turbulent frequency through the following formula.

$$\mu_t = \rho \frac{k}{\omega} \qquad (3)$$

k-equation：

$$\frac{\partial(\rho k)}{\partial t} + \frac{\partial}{\partial x_i}(\rho u_i k) = \frac{\partial}{\partial x_j}\left[\left(\mu + \frac{\mu_t}{\sigma_k}\right)\frac{\partial k}{\partial x_j}\right] + P_k - \beta' \rho k \omega \qquad (4)$$

ω-equation：

$$\frac{\partial(\rho \omega)}{\partial t} + \frac{\partial}{\partial x_i}(\rho u_i \omega) = \frac{\partial}{\partial x_j}\left[\left(\mu + \frac{\mu_t}{\sigma_\omega}\right)\frac{\partial \omega}{\partial x_j}\right] + \alpha \frac{\omega}{k} P_k - \beta \rho \omega^2 \qquad (5)$$

Where P_k represents the rate of generation of turbulence kinetic energy due to viscous effects.

$$P_k = \mu_t \left(\frac{\partial u_i}{\partial x_j} + \frac{\partial u_j}{\partial x_i}\right)\frac{\partial u_i}{\partial x_j} \qquad (6)$$

The model parameters are: β' =0.09, α =5/9, β =0.075, σ_k =2, σ_ω =2.

The main issue with the standard k-ω model is its strong sensitivity to freestream conditions, meaning that minor adjustments to the boundary conditions at the inlet can lead to significant changes in the computational results. To address this problem, Menter made modifications by combining the standard k-ω model near the wall

with the *k-ε* model away from the center region, resulting in the BSL *k-ω* model.

Firstly, improvements were made to the *k-ε* model.

$$\frac{\partial(\rho k)}{\partial t}+\frac{\partial}{\partial x_i}(\rho u_i k)=\frac{\partial}{\partial x_j}\left[\left(\mu+\frac{\mu_t}{\sigma_k}\right)\frac{\partial k}{\partial x_j}\right]+P_k-\beta^{'}\rho k\omega \quad (7)$$

$$\frac{\partial(\rho \omega)}{\partial t}+\frac{\partial}{\partial x_i}(\rho u_i \omega)=\frac{\partial}{\partial x_j}\left[\left(\mu+\frac{\mu_t}{\sigma_\omega}\right)\frac{\partial \omega}{\partial x_j}\right]+2\rho\frac{1}{\sigma_{\omega 2}\omega}\frac{\partial k}{\partial x_j}\frac{\partial \omega}{\partial x_j}+\alpha\frac{\omega}{k}P_k-\beta\rho\omega^2 \quad (8)$$

Define a function: $\phi_3 = F_1\phi_1+(1-F_1)\ \phi_2$, In which ϕ_1 represents the standard *k-ω* model, ϕ_2 represents the improved *k-ε* model, and F_1 is the blending function.

The blending function plays a decisive role in the success of a model, which is based on flow variables and the distance to the nearest surface.

$$F_1=\tanh(\phi_1^4) \quad (9)$$

$$\phi_1=\min\left(\max(\frac{\sqrt{k}}{\beta^{'}\omega y},\frac{500\nu}{y^2\omega}),\frac{4\rho k}{CD_{K\omega}\sigma_{\omega 2}y^2}\right) \quad (10)$$

$$CD_{k\omega}=\max\left(2\rho\frac{1}{\sigma_{\omega 2}\omega}\frac{\partial k}{\partial x_j}\frac{\partial \omega}{\partial x_j},1.0\times10^{-10}\right) \quad (11)$$

Where *y* is the distance to the nearest wall, and *ν* is the kinematic viscosity.

The values of the coefficients in the aforementioned formula are: β' =0.09, α_1 =5/9, β_1 =0.075, σ_{k1} =2, $\sigma_{\omega 1}$ =2, α_2 =0.44, β_2 =0.0828, σ_{k2} =1, $\sigma_{\omega 2}$ =1/0.856.

Although the BSL model combines the advantages of the Wilcox and *k-ε* models, it still cannot accurately predict the onset and quantity of flow separation on smooth surfaces. The main reason is that these models do not consider the transport of turbulent shear stress, which leads to an over-prediction of the eddy viscosity coefficient. By limiting the eddy viscosity coefficient, accurate transport performance can be obtained, which leads to the derivation of the SST *k-ω* model.

$$\nu_t=\frac{a_1 k}{\max(a_1\omega,SF_2)} \quad (12)$$

$$\nu_t=\mu_t/\rho \quad (13)$$

Where F_2 constrains the boundary layer near the wall and compensates for the incorrect basic assumptions when it comes to free shear flows. *S* is an invariant of the strain rate.

$$F_2=\tanh(\phi_2^2) \quad (14)$$

$$\phi_2=\max(\frac{2\sqrt{k}}{\beta^{'}\omega y},\frac{500\nu}{y^2\omega}) \quad (15)$$

Where *y* is the distance to the nearest wall, and *ν* is the kinematic viscosity.

1.3.Cavitation model

The Rayleigh-Plesset cavitation model is employed, and the Rayleigh-Plesset equation describes the inception, growth, and collapse of vapor bubbles in the fluid.

$$R_b \frac{d^2 R_b}{dt^2} + \frac{3}{2}\left(\frac{dR_b}{dt}\right)^2 + \frac{2\sigma}{\rho_l R_b} = \frac{p_b - p}{\rho_l} - \frac{4\mu_l}{\rho_l R_b}\frac{dR_b}{dt} \quad (16)$$

Where R_b represents the vapor bubble radius, σ is the surface tension coefficient between the liquid and gas phases, ρ_l is the fluid density, p_b is the pressure inside the vapor bubble (assuming the temperature of the vapor bubble is the same as that of the liquid), p is the pressure of the liquid surrounding the vapor bubble, and μ_l is the liquid dynamic viscosity. The equation assumes that the fluid density and turbulent viscosity remain constant, and there is no thermal resistance during the vapor bubble growth process.

Ignoring the second-order differential term, the effects of surface tension and viscous drag, as well as buoyancy, the Rayleigh-Plesset equation can be simplified.

$$\frac{dR_b}{dt} = \sqrt{\frac{2}{3}\frac{p_b - p}{\rho_l}} \quad (17)$$

It is assumed that the growth of a vapor bubble starts from an initial average bubble radius and that it collapses back to its original size. f_v represents that the number of cavitation bubbles per unit volume can be expressed through the volume fraction of the gas phase. N_b represents the number of cavitation bubbles per unit volume.

$$N_b = \frac{3 f_v}{4\pi R_b^3} \quad (18)$$

The vaporization process f_v is replaced by $f_n(1\text{-}f_v)$, where f_n is the volume fraction at the nucleation sites.

The rate of change of vapor bubble mass is as follows:

$$\frac{dm_b}{dt} = \rho_b \frac{dV_b}{dt} = 4\pi R_b^2 \sqrt{\frac{2}{3}\frac{p_v - p}{\rho_l}} \quad (19)$$

Ultimately, the overall mass phase change rate per unit volume can be derived.

$$m_{lv} = N_b \frac{dm_b}{dt} = F\frac{3 f_v \rho_b}{R_b}\sqrt{\frac{2}{3}\frac{|p_v - p|}{\rho_l}}\,\mathrm{sgn}\left(p_v - p\right) \quad (20)$$

Where F is an empirical coefficient derived from experiments, which represents different values under condensing and vaporizing conditions. When calculating cavitation issues in CFX, the Rayleigh-Plesset model is referenced, which provides default model parameters such as: R_b =1μm, f_n =5×10^{-4}, the vaporization coefficient F_v =50, and the condensation coefficient F_c =0.01. These parameters have been validated by a multitude of fundamental research studies.

2. Experimental Setup

The external characteristics experiment of the high-speed centrifugal pump was conducted on a closed test rig. Fig. 1 is the schematic diagram of the closed test rig structure.

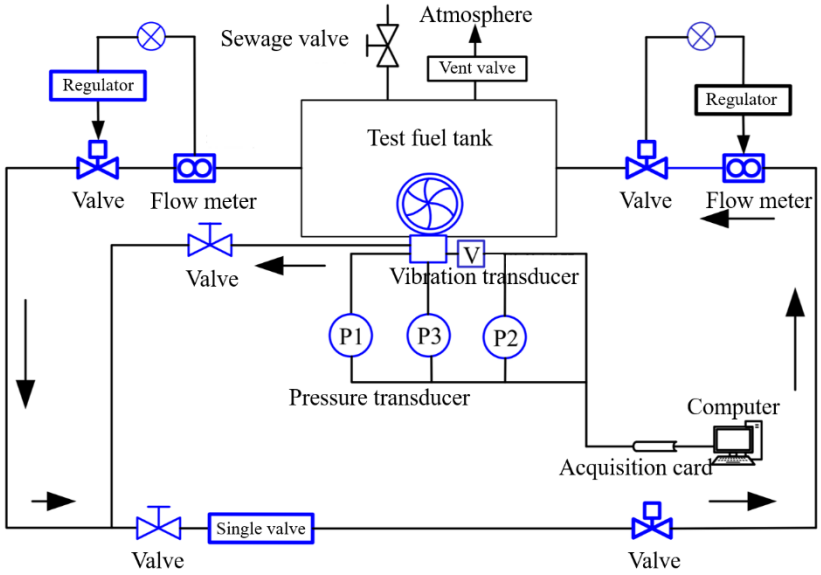

Figure 1. Schematic diagram of the closed test bench structure

The experimental system mainly consists of valves, flow meters, regulators, test fuel tank, vibration transducer, pressure transducer, acquisition card and computer.

In this experiment, the integrated induced impeller centrifugal pump was selected for testing at full flow rate conditions before cavitation occurred to primarily obtain the pump's external characteristic data. The external characteristic data of the integrated induced impeller centrifugal pump was input into the computer through a data acquisition card, followed by processing the experimental data and comparing it with the numerical simulation results.

3. Research Object

The subject of this study is a certain high-speed centrifugal pump, which mainly consists of the inflow section, impeller area, guide vane, volute, and outflow section. Fig. 2 is the Isometric drawing of centrifugal pump, Fig. 3 is the drawing of integrated induced impeller fluid domain, Fig. 4 is the drawing of inducer-impeller fluid domain. The main parameters of pump model are listed in the Table 1.

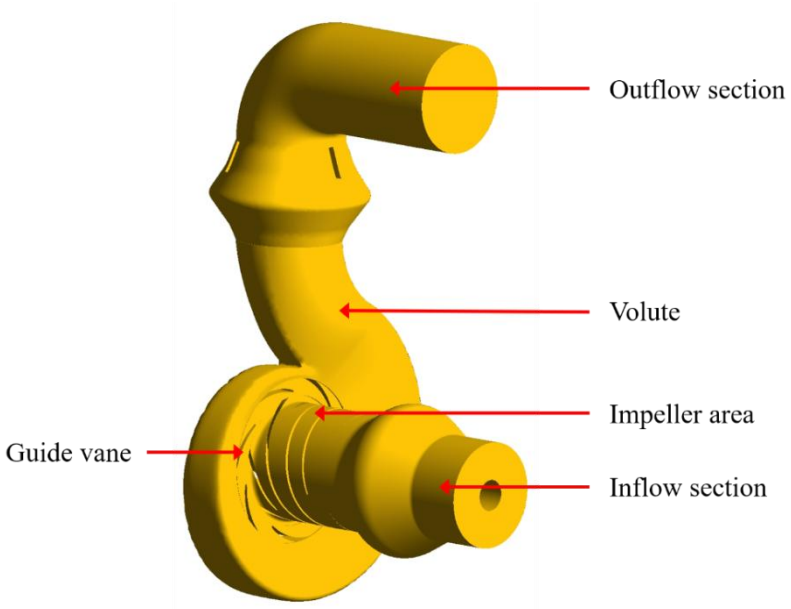

Figure 2. Isometric drawing of centrifugal pump

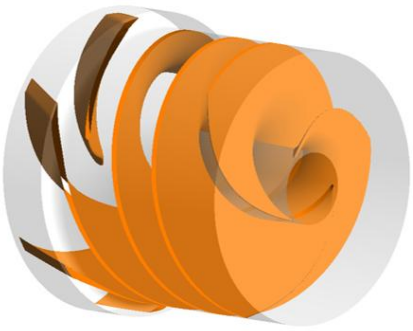

Fig. 3. Drawing of integrated induced impeller fluid domain

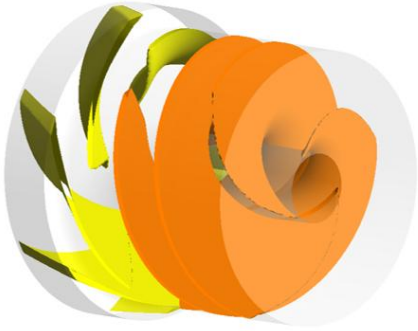

Fig. 4. Drawing of inducer-impeller fluid domain

Table 1 Main parameters of the objective pump.

Parameters	Value	Unit
Design head H_d	19	[m]
Design flow rate Q_d	800	[L/min]
Rated speed of impeller n_d	7800	[r/min]
Cavitation specific speed C	5000	[-]
Specific speed n_s	356	[r/min]
Diameter of the impeller outlet edge D_{i2}	72	[mm]
Axial length of integrated induced impeller L_1	75	[mm]
Axial length of inducer-impeller L_2	75	[mm]
Number of long blades of integrated induced impeller Z_{long}	3	[-]
Number of long blades of integrated induced impeller Z_{short}	3	[-]
Number of blades of inducer Z_{ind}	3	[-]
Number of blades of impeller Z_{imp}	6	[-]

Table 2 Grid number of each parts.

Component	Mesh element type	Mesh node number
Inflow section	Hexahedral structured mesh	382530
Integrated induced impeller	Tetrahedral unstructured mesh	2630174
Inducer-impeller	Tetrahedral unstructured mesh	2996165
Guide vane	Tetrahedral unstructured mesh	684255
Volute	Tetrahedral unstructured mesh	126153
Outflow section	Tetrahedral unstructured mesh	251844

ICEM CFD is used to mesh the fluid domain. Fig. 5 is Integrated induced impeller mesh situation. Fig. 6 is Inducer-impeller mesh situation. The number of grids in each part is shown in the Table 2.

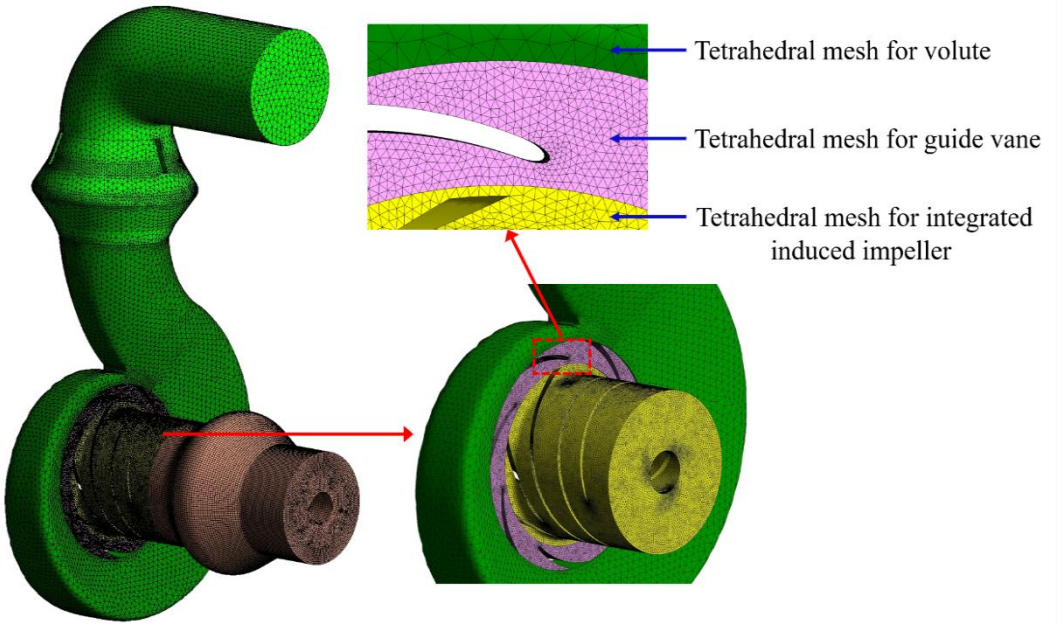

Figure 5 Integrated induced impeller mesh situation

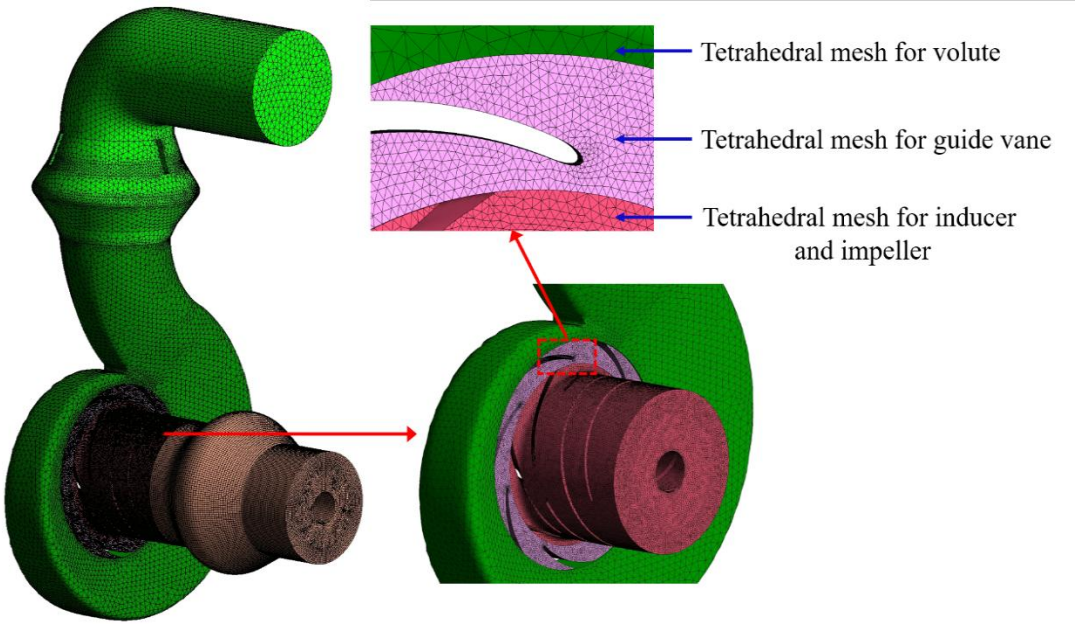

Figure 6 Inducer-impeller mesh situation

4. Setup of the Numerical Simulation and Experimental Validation

4.1. Setup of the Numerical Simulation

In this CFD design process, the inlet boundary condition is set to total pressure, which varies with the calculation settings. The outlet boundary condition is set to mass flow. Among all the components of the pump, the integrated impeller and the inducer-impeller are set as rotating domains with a rotational speed of 7800 rpm, while the remaining components are stationary. The walls are set as non-slip walls. Data transfer interfaces are set at the connections between each of the flow components. The reference pressure is 0 Pa, and the working condition is at 25°C. The fluid medium density inside the centrifugal pump is 780 kg/m³ and the molar mass of 167.31 kg/kmol. In this project's calculations, the saturated vapor pressure of the gas medium, p_v is set to 1000 Pa. The liquid phase volume fraction at the inlet boundary is set to 1, and the gas phase volume fraction is set to 0.

4.2.Experimental Validation

In this section, a comparison is made between the numerical simulation results and the experimental results of the research object. Fig.

7 shows the comparison curve of head, and it is found that under the design flow condition, the experimental data of the integrated induced impeller matches well with the numerical simulation results, making the numerical results fully reliable. It can also be observed that the head of the inducer-impeller is significantly higher than that of the integrated induced impeller. Fig. 8 is the efficiency comparison curve, which shows that the efficiency of the integrated induced impeller is clearly superior to that of the inducer-impeller.

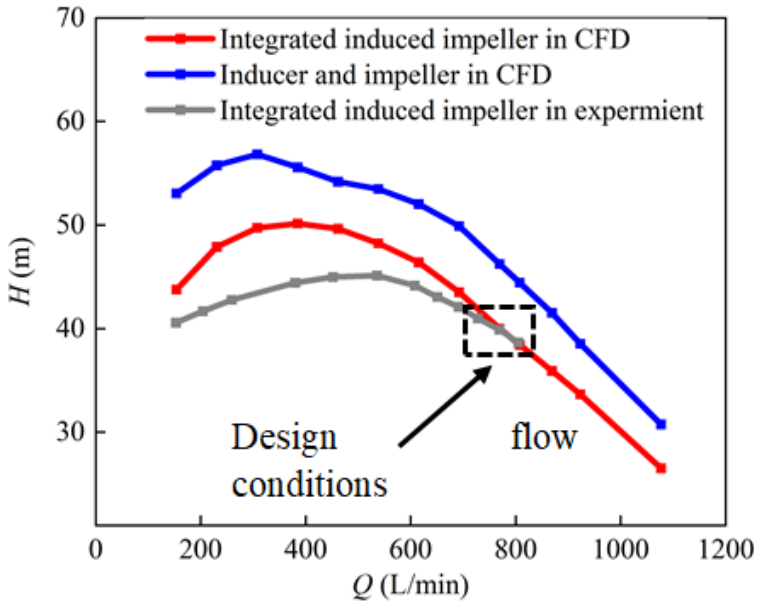

Figure 7 Comparison curve of head

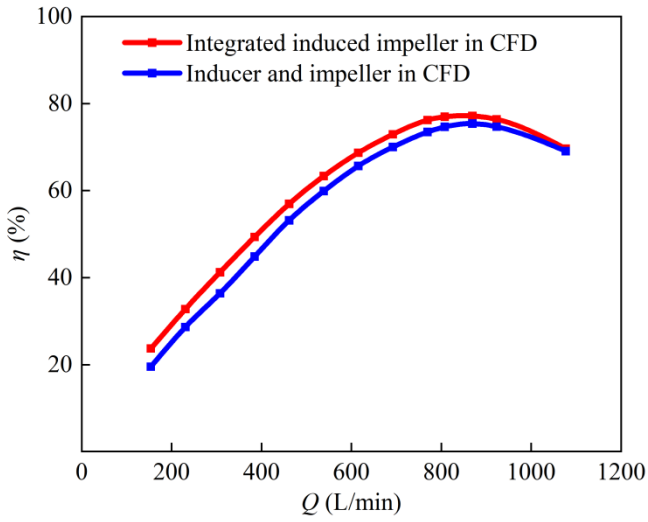

Figure 8 Comparison curve of efficiency

5. Cavitation Performance

5.1.Dimensionless Parameters

In this study, each parameter has different units of measurement, which complicates the analysis of parameters. Therefore, this section will define the dimensionless parameters used in this research.

As the total pressure at the inlet of the centrifugal pump decreases, the cavitation level of the centrifugal pump gradually intensifies, and the efficiency of the centrifugal pump noticeably decreases. The cavitation number σ can reveal the cavitation performance of the centrifugal pump. The expression for cavitation number σ is:

$$\sigma = \frac{(p_0 - p_v)C_{cav}}{\frac{1}{2}\rho v_0^2} \quad (21)$$

Where p_0 is the pressure at the inlet of the centrifugal pump, u_0 is the peripheral speed at the intersection of the impeller inlet edge and the front shroud, p_v is 1000Pa, C_{cav} =1000.

$$v_0 = \frac{n\pi D}{60} \quad (22)$$

Where D is the diameter at the intersection of the impeller inlet edge and the front shroud (unit is mm), n is the impeller rotational speed, with n =7800 r/min.

At the same time, the dimensionless parameter C_p is defined as the pressure coefficient representing the flow field pressure value.

$$C_p = \frac{2(p - p_{in})}{\rho v_{in}^2} \quad (23)$$

Where p is the pressure value, p_{in} is the pressure at the inlet of the centrifugal pump, v_{in} is the velocity of the fluid at the inlet of the centrifugal pump.

5.2.Cavitation Characteristic Curve

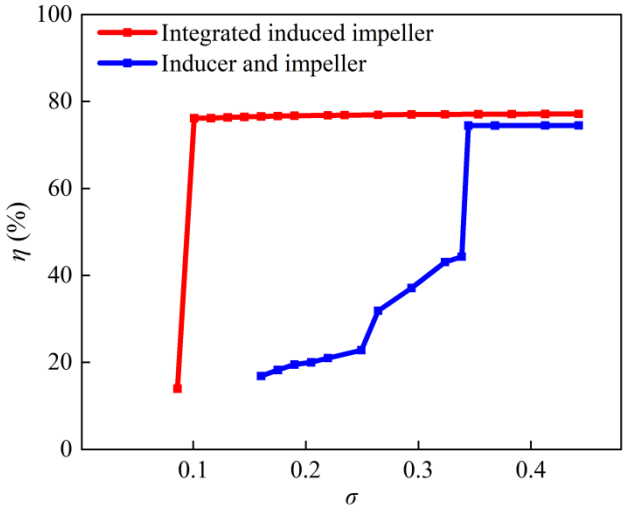

Figure 9 Cavitation characteristic curve

Fig. 9 shows the cavitation characteristic curves of the integrated induced impeller and the inducer-impeller obtained from CFD numerical simulation. From the figure, it can be seen that the entire cavitation characteristic curve can be divided into the following stages based on the change in efficiency: the initial cavitation stage where the efficiency does not change significantly, and the fully developed cavitation stage where the decrease in cavitation number causes the efficiency to drop rapidly. The cavitation number at which the cavitation characteristic curve of the integrated induced impeller enters the fully cavitated stage is lower than that of the inducer-impeller cavitation characteristic curve. Overall, the efficiency of the integrated induced impeller is higher than that of the inducer-impeller, and the cavitation performance of the integrated induced impeller is significantly better than that of the inducer-impeller.

5.3.Analysis of Cavitation Mechanisms

5.3.1. The Causes and Mechanisms of

Cavitation Formation

It is well known that the pressure distribution on the blades of a centrifugal pump plays a crucial role in cavitation. When the pressure on the centrifugal pump blades drops below the saturation vapor pressure of the fluid, bubbles or groups of bubbles are formed. These bubbles flow with the fluid and may collapse in high-pressure areas, eventually leading to cavitation. When the σ of the integrated induced impeller is 0.086, the circumferential pressure load distribution at the tip of the short blades is shown in Fig. 10. The area enclosed by the load distribution curve between the pressure side and the suction side of the blade represents the magnitude of the pressure difference between these two sides. This area quantifies the pressure differential experienced between the pressure side and the suction side of the blade. When cavitation occurs to a certain extent, the efficiency of both the integrated induced impeller and the inducer-impeller decreases.

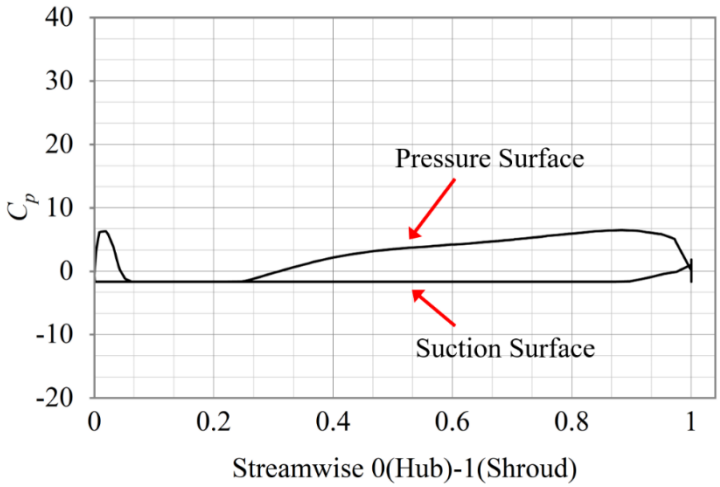

Figure 10. C_p distribution of blade at σ =0.086

5.3.2. Cavitation Analysis

As the pressure on the centrifugal pump blades gradually decreases, the cavitation number σ decreases correspondingly, and the scale of cavitation inside the centrifugal pump increases gradually. To visually display the development of cavitation within the integrated induced impeller and the inducer-impeller, a 3D perspective view of the entire flow path of the centrifugal pump is presented to observe the distribution of gas under different cavitation numbers within the impeller.

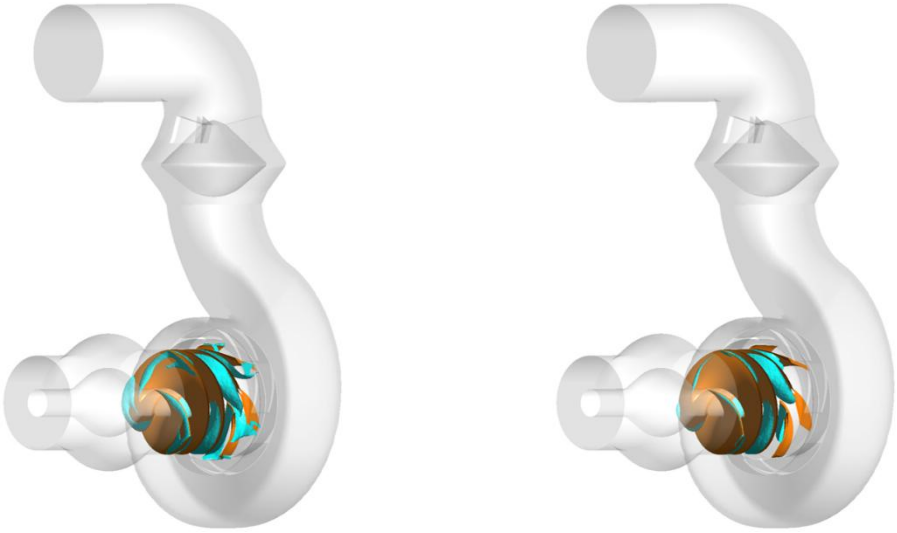

(a) σ =0.086 (b) σ =0.101

(c) σ =0.145 (d) σ =0.353

Figure 11. Transparent view of the integrated induced impeller

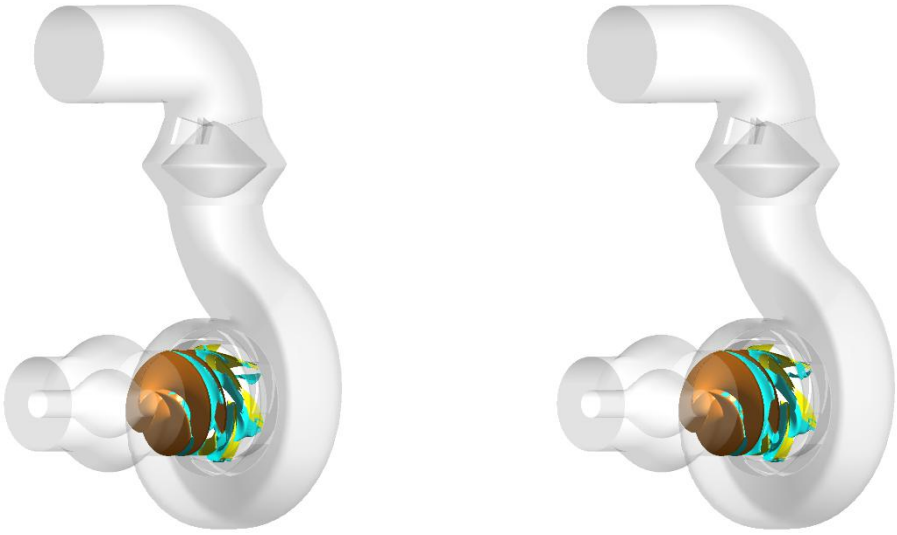

(a) σ =0.249 (b) σ =0.338

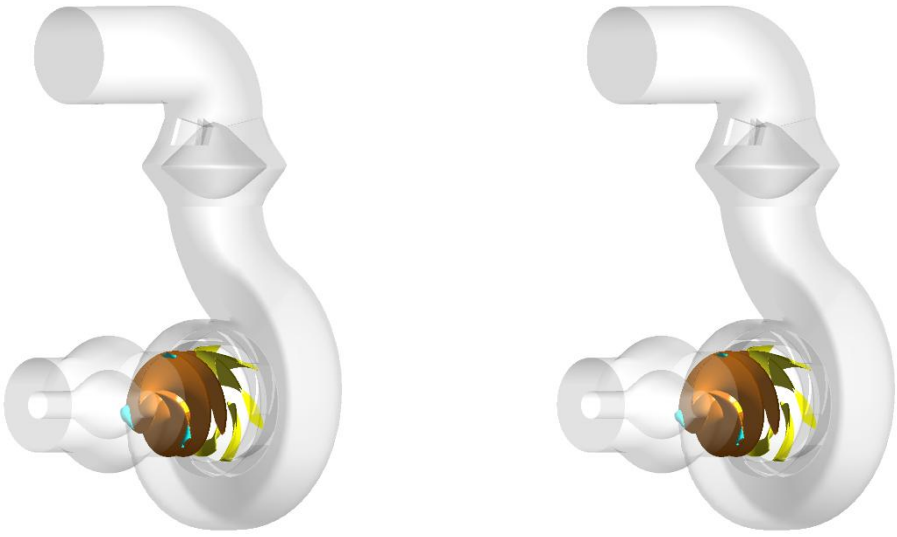

(c) σ =0.344 (d) σ =0.412

Figure 12. Transparent view of the inducer-impeller

Fig.11 shows the vapor distribution when the cavitation number σ of the integrated induced impeller is 0.086, 0.101, 0.145, and 0.353, and the vapor volume percentage is 3%. It is evident that cavitation has occurred in the integrated induced impeller when σ =0.086, with the vapor mainly concentrated on the pressure and suction sides of the long blades of the integrated induced impeller. The vapor distribution is discontinuous at the inlet edge of the long blades, and a large amount of vapor fills the area between the long and short blades, attaching to the inlet edge of the short blades. As the cavitation number increases, the vapor volume distribution within the integrated induced impeller decreases, with significant reductions at the inlet edges of the long and short blades. The vapor still primarily concentrates on the pressure and suction sides of the long blades, which is closely related to the pressure difference between these surfaces. With a further increase in the cavitation number, the vapor distribution appears at the inlet edge of the long blades and decreases as the cavitation number increases.

Comparing the inducer-impeller with the integrated induced impeller, Fig.12 show the vapor distribution when the cavitation number of the inducer-impeller is 0.249, 0.338, 0.344, and 0.412, with a vapor volume percentage of 3%. When cavitation occurs in the inducer-impeller (σ =0.249), the gas is mainly distributed inside the inducer and at the junction between the inducer and the impeller, with some vapor attachment on the impeller blades, but almost no vapor distribution at the inlet edge of the inducer. As the cavitation number increases, the vapor volume distribution decreases. With a further increase in the cavitation number (σ =0.344), the vapor distribution shifts towards the inlet of the inducer, with almost no vapor distribution inside the inducer and the impeller.

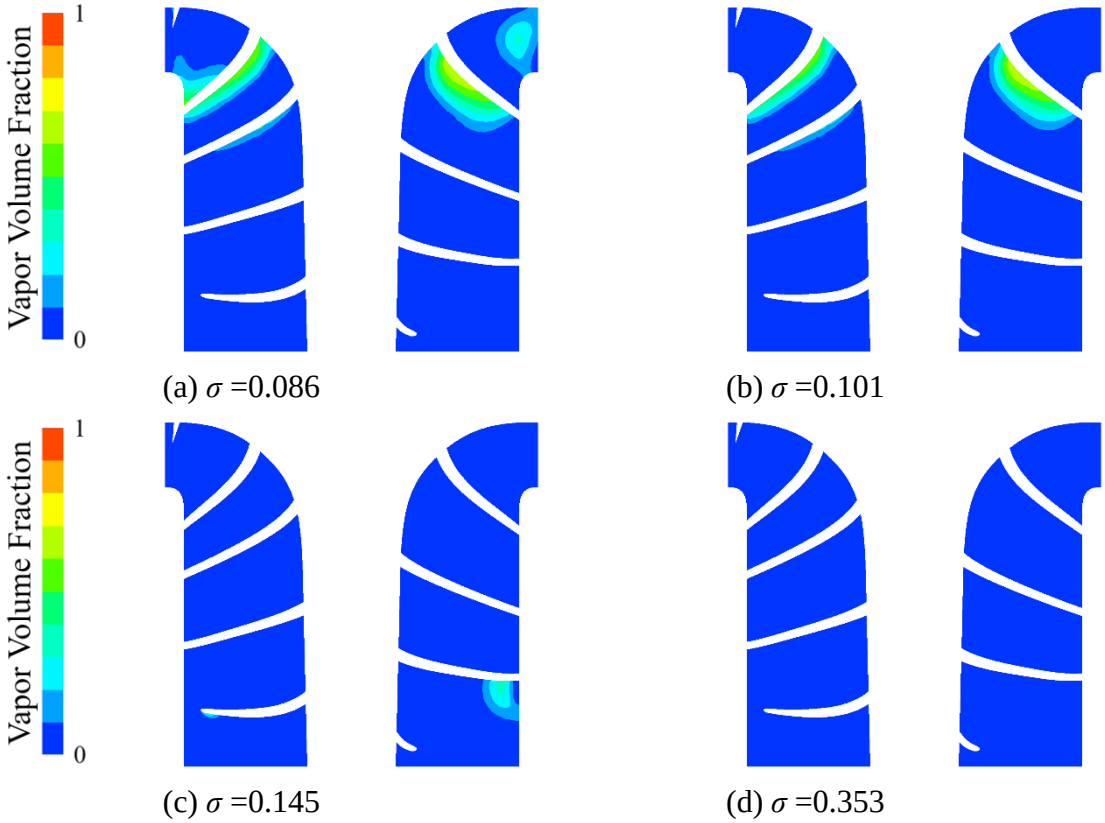

(a) σ =0.086 (b) σ =0.101

(c) σ =0.145 (d) σ =0.353

Figure 13. Vapor volume fraction distribution on the integrated induced impeller

To further illustrate the internal vapor distribution of the integrated induced impeller and the inducer-impeller, Fig. 13 is vapor volume fraction distribution on the integrated induced impeller. At a cavitation number σ of 0.086, cavitation begins on the surface of the short blades and the outlet surface of the long blades, gradually diffusing outward. The pressure and suction sides of the short blades both have cavitation areas, but the suction side's cavitation area is larger than the pressure side's; the cavitation area on the suction side of the long blades is more pronounced and

decreases along the direction opposite to the fluid flow, with a significant reduction in the area, while the pressure side has almost no cavitation area; a circular cavitation area exists at the junction of the short blades and the front shroud. When the cavitation number σ is 0.101, the cavitation area decreases, the circular cavitation area disappears, and the overall position of the cavitation area does not change significantly. When the cavitation number σ is 0.145, the cavitation area shifts to the inlet edge of the integrated induced impeller near the hub, with the cavitation area concentrated on the suction side of the impeller, and no cavitation area on the pressure side. With a further increase in the cavitation number, there is almost no gas distribution within the integrated induced impeller.

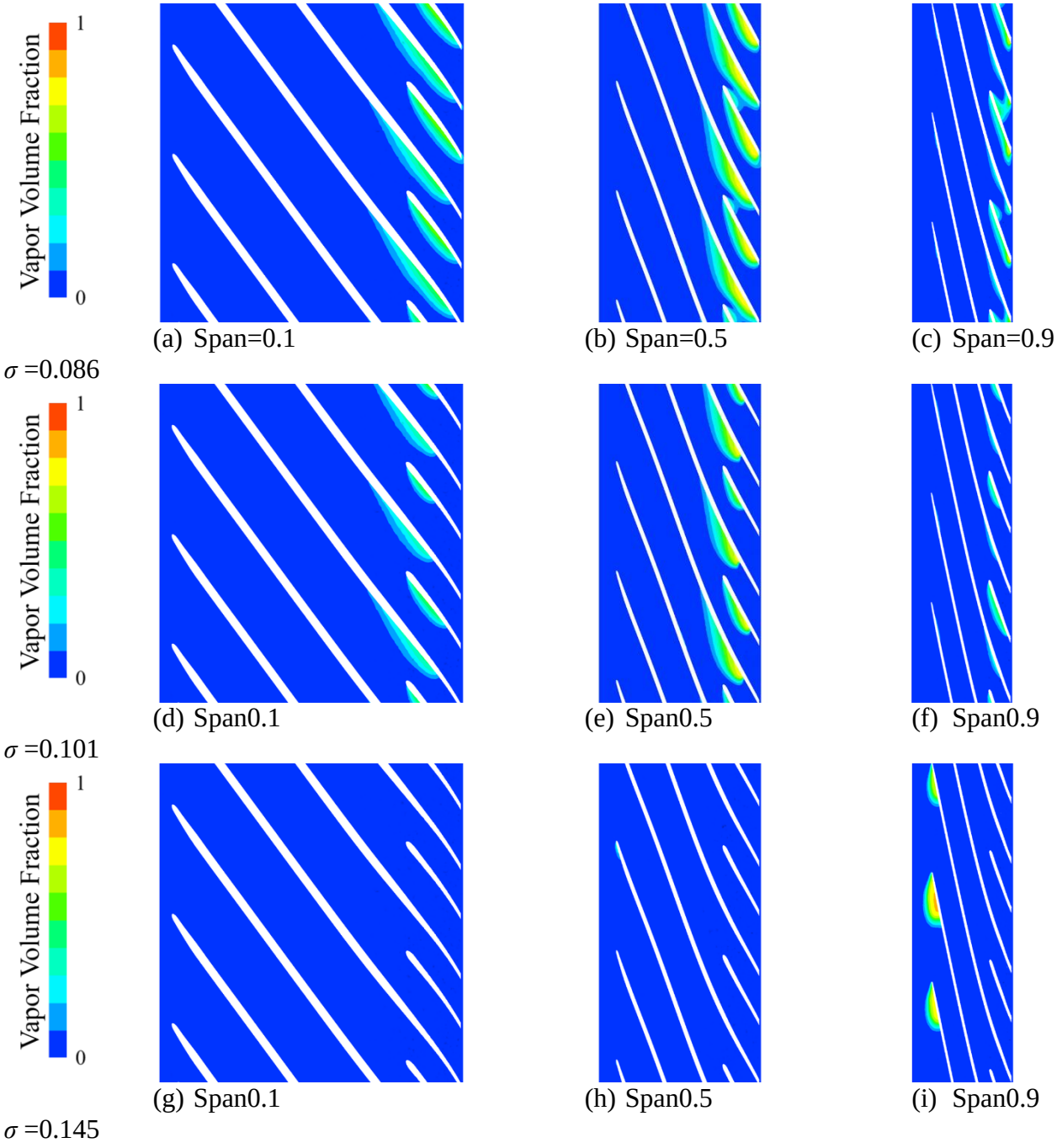

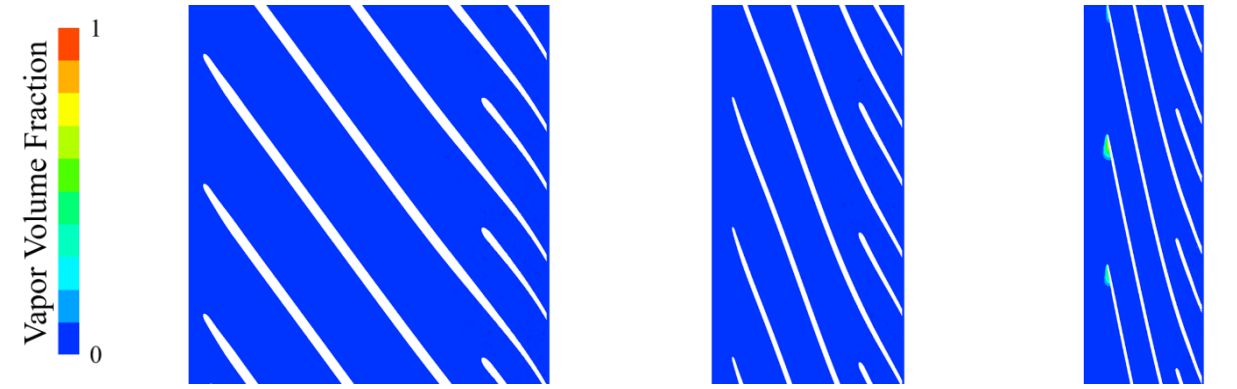

Figure 14. Contour of vapor volume fraction for the integrated induced impeller

Fig. 14 shows the vapor volume fraction distribution on different spanwise surfaces for the integrated induced impeller at various cavitation numbers. At a cavitation number σ of 0.101, the cavitation region begins at the surface of the short blades and the outlet surface of the long blades and gradually spreads outward. The pressure and suction sides of the short blades both have cavitation areas, but the suction side's cavitation area is larger than the pressure side's cavitation area. The cavitation area on the suction side of the long blades is more pronounced and decreases along the direction opposite to the fluid flow, with a significant reduction in the area. The pressure side has almost no cavitation area. A circular cavitation area exists at the junction of the short blades and the front shroud. When the cavitation number decreases to σ =0.086, the cavitation area increases, and the circular cavitation area disappears. The overall position of the cavitation area does not change significantly. As the cavitation number σ increases to 0.145, the cavitation area shifts to the inlet edge of the integrated induced impeller, with the cavity attaching to the suction side of the long blades. With a further increase in the cavitation number, the cavitation area decreases. It is preliminarily proposed that as the cavitation number decreases, the cavitation scale on the suction side of the long blades of the integrated induced impeller gradually increases and moves towards the outlet. Cavitation occurs on both the pressure and suction sides of the short blades, and under the drive of blade pressure, the cavity tends to spread from the suction side of the long blades to the adjacent pressure side of the short blades. When the cavitation number drops to a certain extent, the pressure side of the adjacent short blades begins to cavitate.

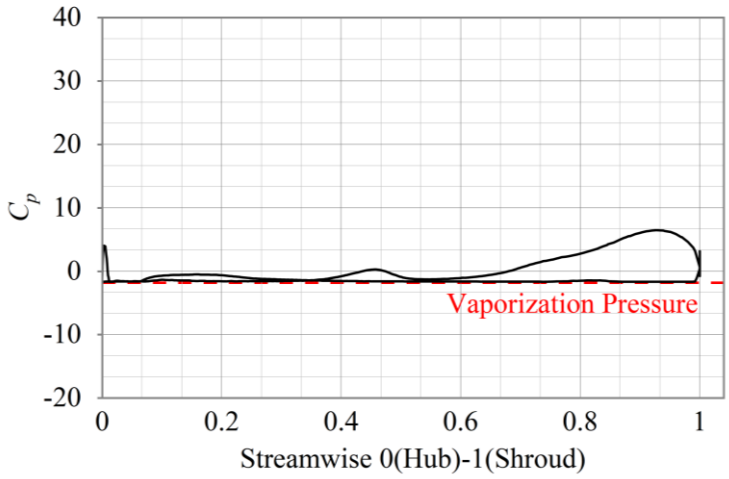

(a) σ =0.086 the long blade

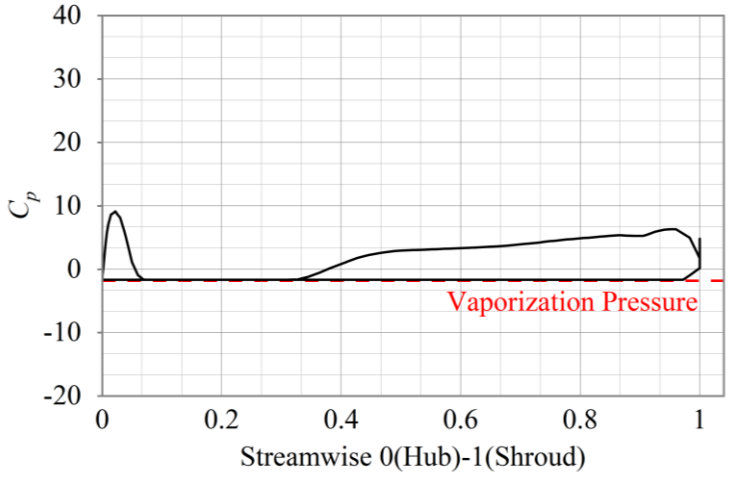

(b) σ =0.086 the short blade

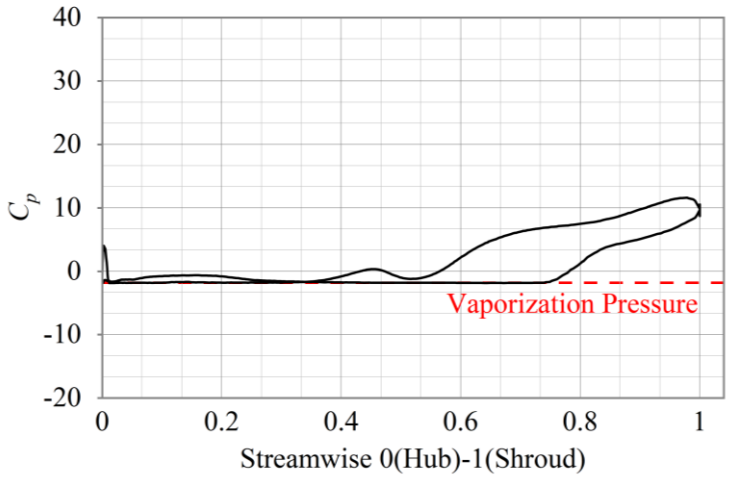

(c) σ =0.101 the long blade

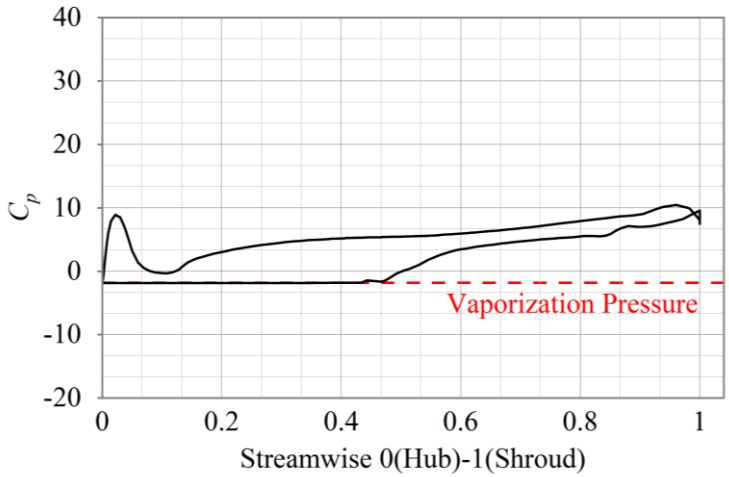

(d) σ =0.101 the short blade

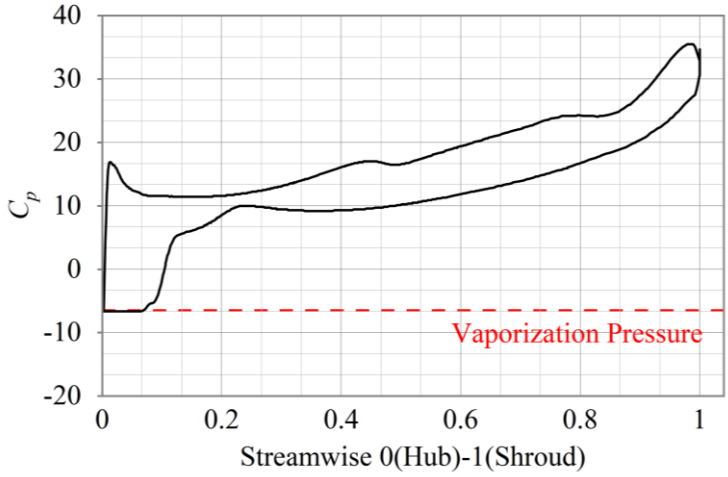

(e) σ =0.145 the long blade

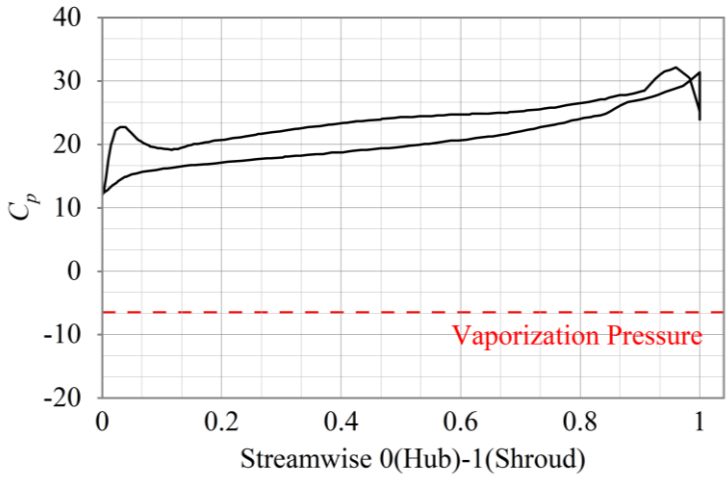

(f) σ =0.145 the short blade

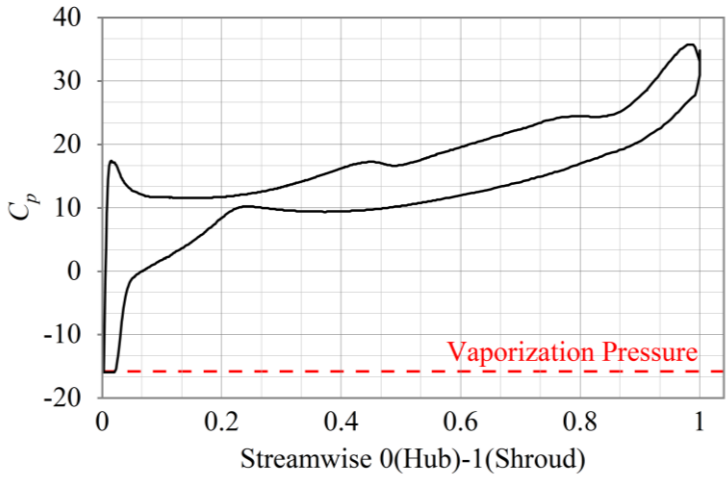

(g) σ =0.353 the long blade

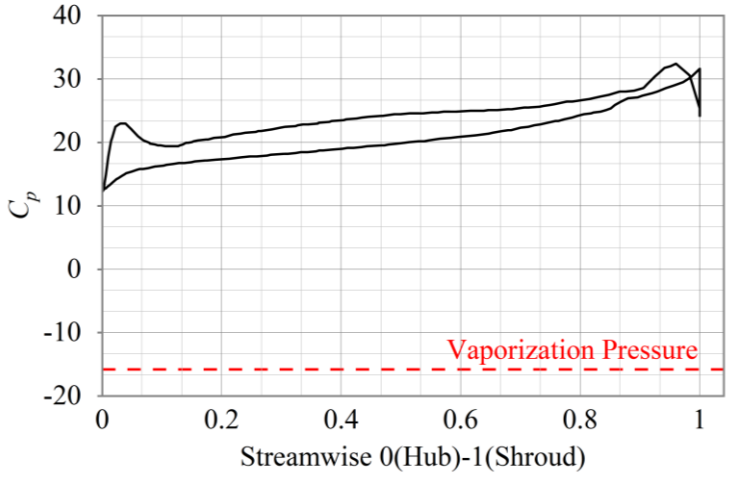

(h) σ =0.353 the short blade

Figure 15 The pressure load distribution on the blades of the integrated induced impeller

Fig. 15 shows the expansion at span 0.9 for the same long and short blades. At σ =0.353, which is the initial stage of cavitation, no cavitation is observed on the short blades, while there are a few cavitation areas on the long blades. When σ =0.353, the cavitation areas on the long blades increase, and further cavitation occurs, with the cavitation areas concentrated on the suction side of the long blades and near the impeller inlet. There are no further changes in cavitation on the short blades. As the cavitation number decreases, at σ =0.101, most of the long blades have cavitated, with less cavitation on the working surface compared to the suction surface. The cavitation areas are mainly concentrated in the middle of the integrated induced impeller. At this time, the short blades also cavitate, with no cavitation on the pressure side of the short blades, but about half of the suction side is cavitated. At σ =0.086, the integrated induced impeller has completely cavitated. Changes in pressure on the blade surface cause the formation of cavitation areas, which occur when the pressure on the blade surface is lower than the fluid's saturation vapor pressure. As the cavitation number decreases, the area enclosed by the pressure surface pressure curve and the suction surface pressure curve decreases, representing the increase in pressure value. The occurrence of cavitation leads to a reduction in the integrated induced impeller's pressure increase value, which further affects the integrated induced impeller's working performance.

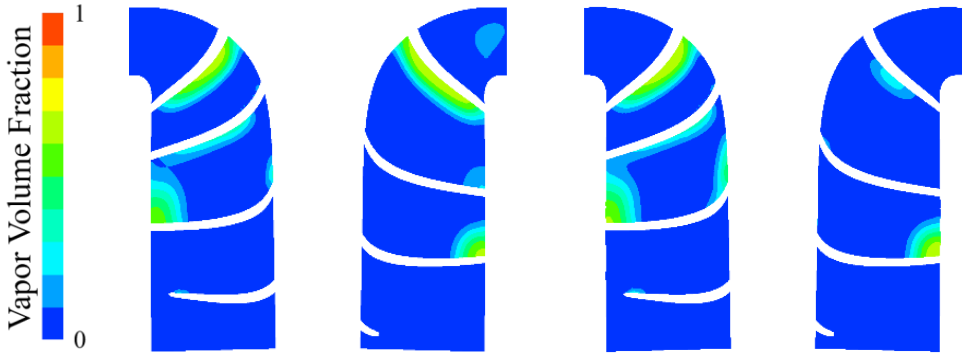

(a) σ =0.249 (b) σ =0.338

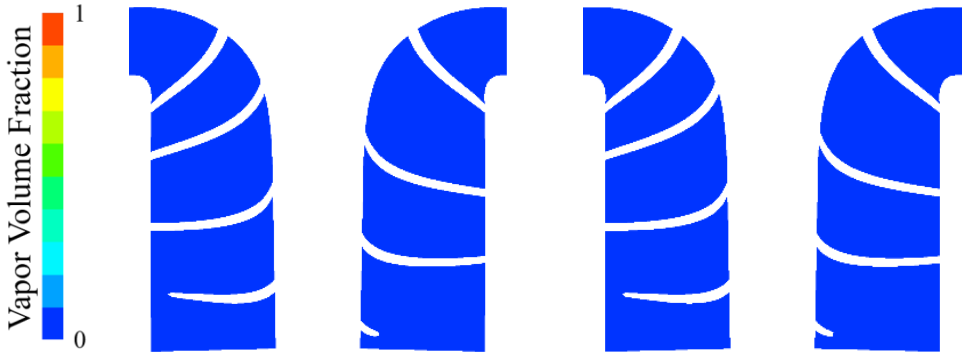

(c) σ =0.344 (d) σ =0.412

Figure 16. Vapor volume fraction distribution on the inducer-impeller

Fig. 16 illustrates the vapor volume fraction distribution on the inducer-impeller. At a cavitation number σ of 0.249, cavitation occurs in both the inducer and the impeller, with the cavitation regions primarily on the pressure side of the inducer and minor cavitation on the suction side. Concurrently, the cavities on the suction side of the inducer connect with those on the pressure side, blocking the flow channel. As the cavitation number increases, at σ =0.338, the cavitation area within the flow channel decreases, but the area of the connected cavities increases. At cavitation numbers σ =0.344 and σ =0.412, no cavitation is observed within the inducer and impeller.

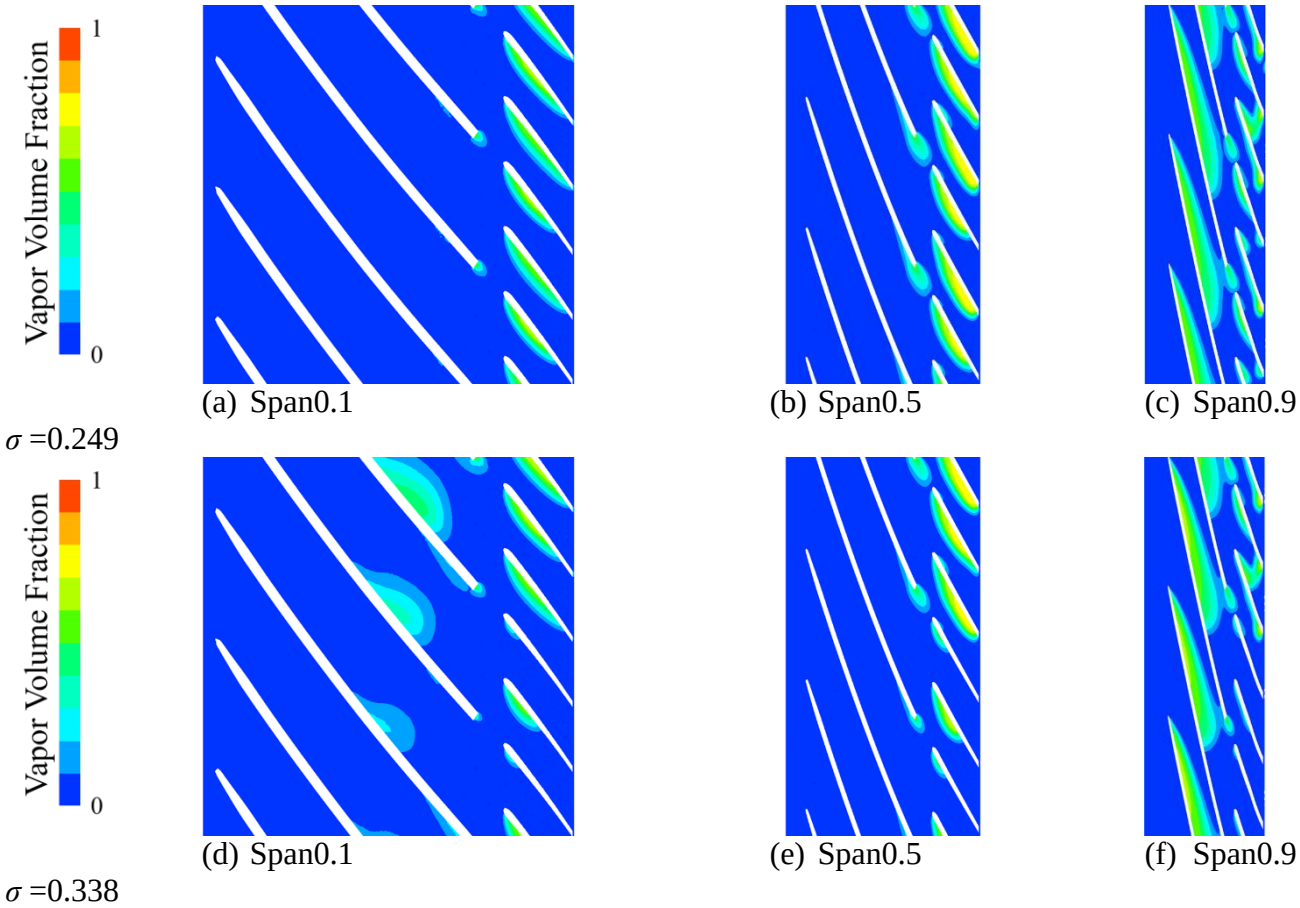

(a) Span0.1 (b) Span0.5 (c) Span0.9

σ =0.249

(d) Span0.1 (e) Span0.5 (f) Span0.9

σ =0.338

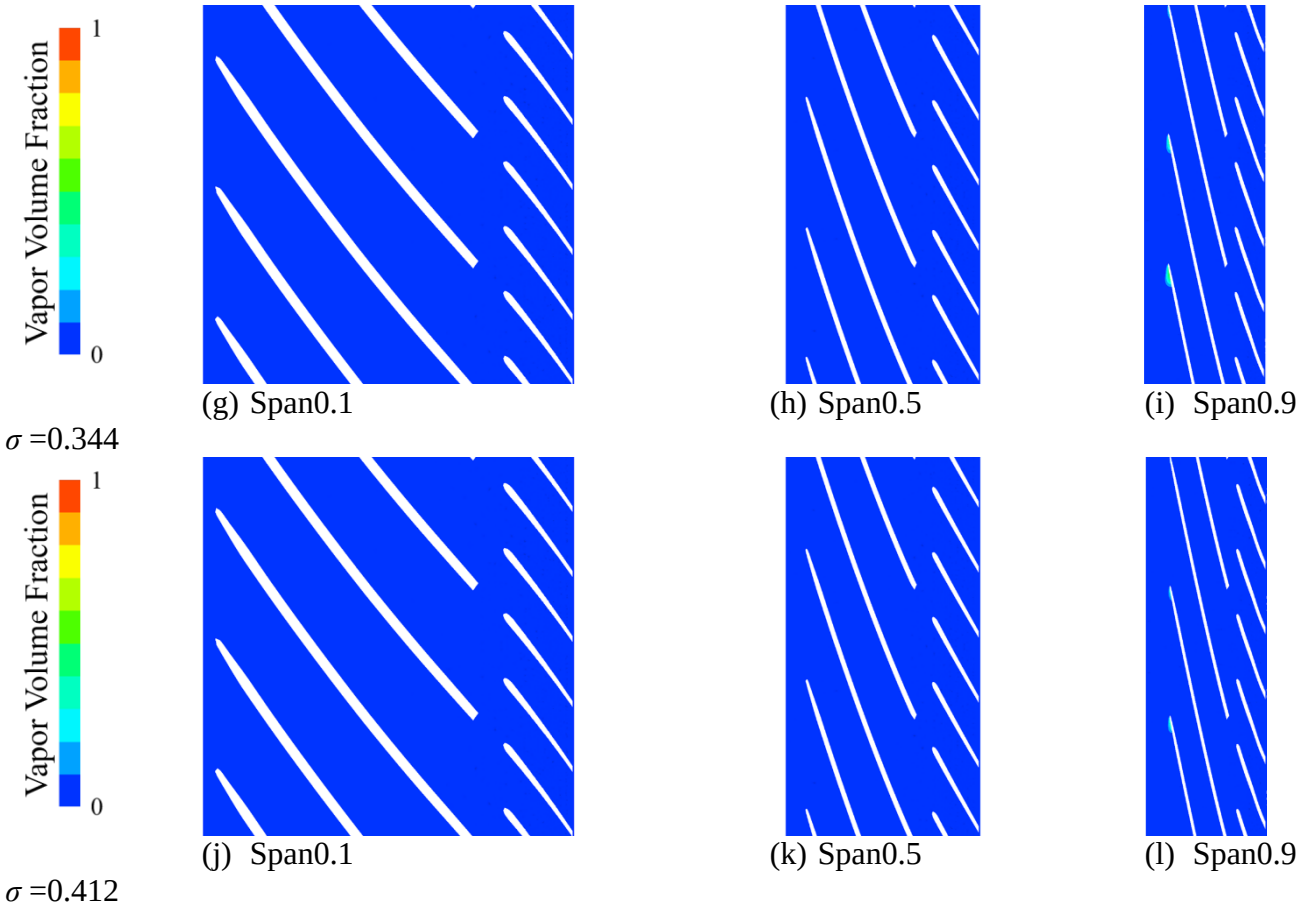

Figure 17. Contour of vapor volume fraction for the inducer-impeller

Fig. 17 depicts the contour of vapor volume fraction for the inducer-impeller at different cavitation numbers. At σ =0.249, it is evident that at span0.9, there is a significant occurrence of cavitation on the pressure side of the inducer, with cavities on the pressure side connecting to those on the suction side. Similarly, cavities on the pressure side of the impeller connect with those on the suction side, and cavitation regions form at the gap between the inducer and the impeller. At the same cavitation number, the cavitation areas on the inducer are considerably smaller at span0.1 and span0.5 compared to span0.9, with some cavitation regions present at the outlet of the inducer, and the cavitation areas on the impeller are orderly, concentrated on the suction side of the impeller. As the cavitation number increases to σ =0.338, the cavitation on the pressure surface of the inducer appears in a teardrop shape, and the cavitation areas on the impeller decrease compared to σ =0.249. With a further increase in the cavitation number, the cavitation regions within the inducer and impeller are significantly reduced. At span0.9, cavitation occurs on the suction side near the inlet of the inducer, but the cavitation area is minimal.

In comparison, the integrated induced impeller shows better cavitation performance than the inducer-impeller. When cavitation occurs in the integrated induced impeller, the cavities within the impeller are orderly and rarely connect to block the flow channel. In contrast, when cavitation occurs in the inducer-impeller, there are multiple connected cavities, and cavitation also occurs at the gap between the inducer and the impeller, which further impedes fluid flow and affects the impeller's performance.

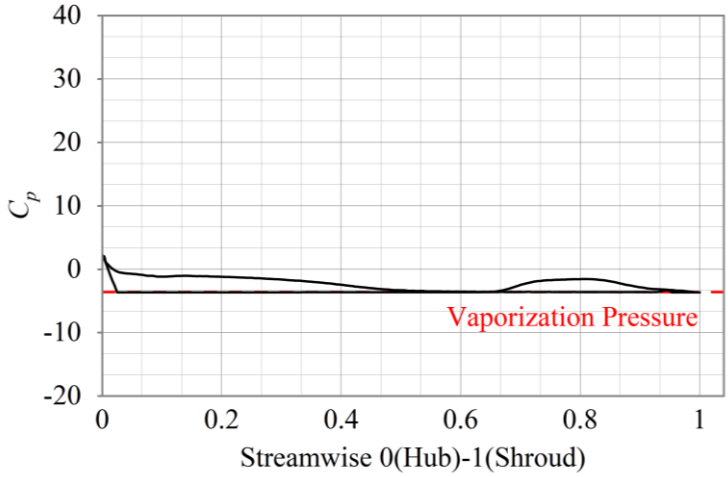

(a) σ =0.249 the inducer blade

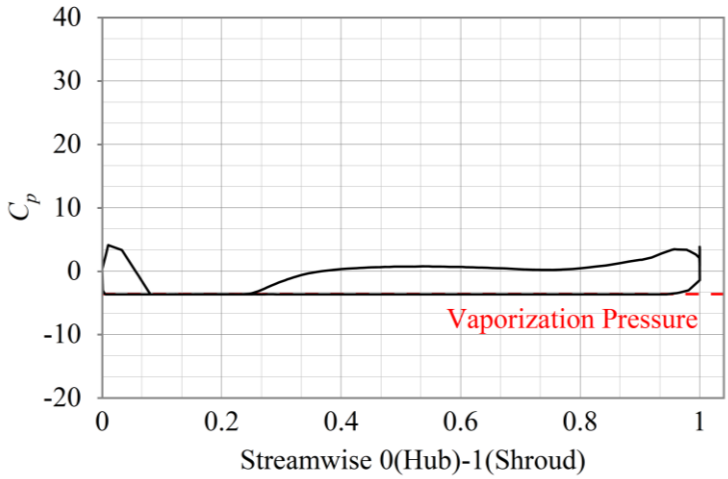

(b) σ =0.249 the impeller blade

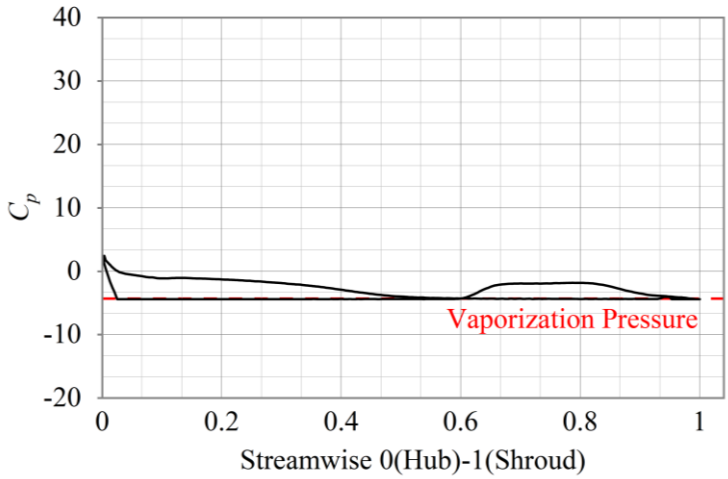

(c) σ =0.338 the inducer blade

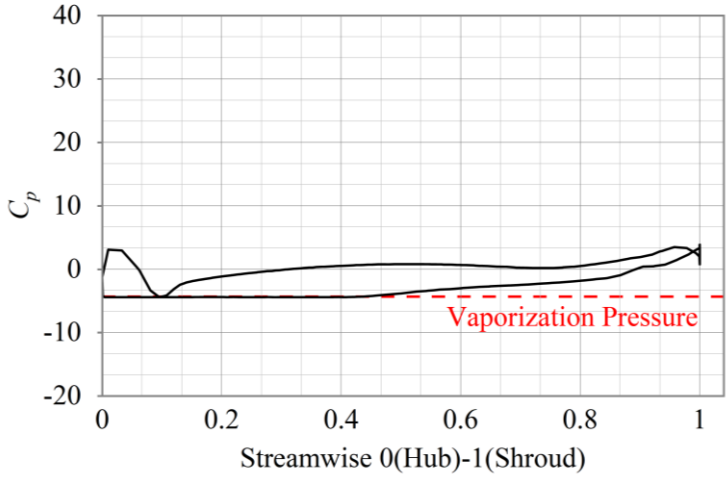

(d) σ =0.338 the impeller blade

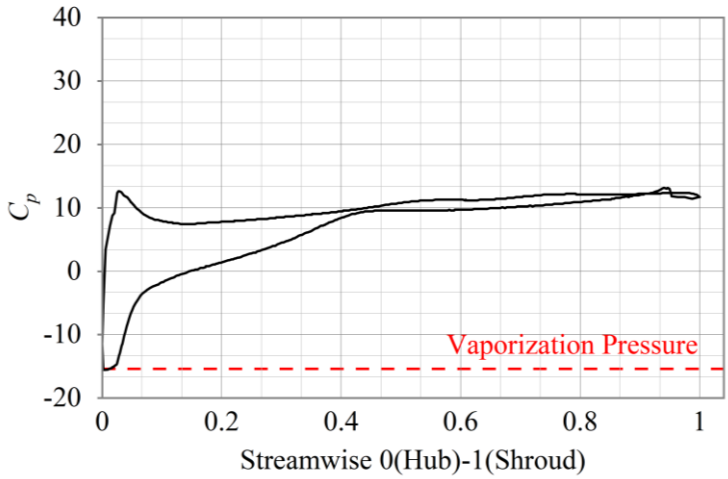

(e) σ =0.344 the inducer blade

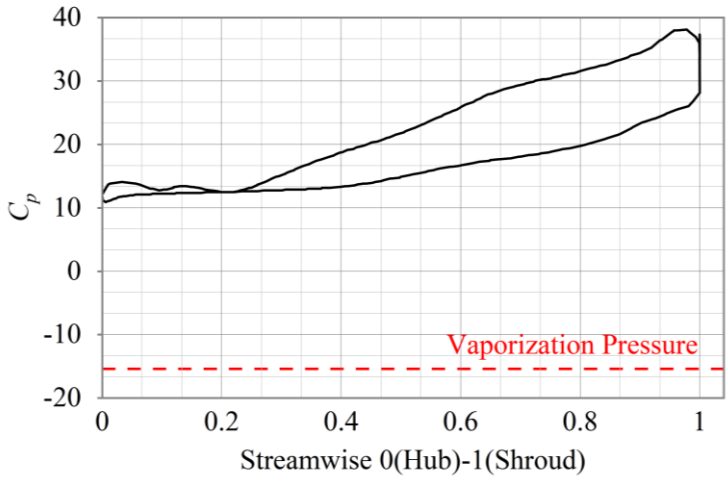

(f) σ =0.344 the impeller blade

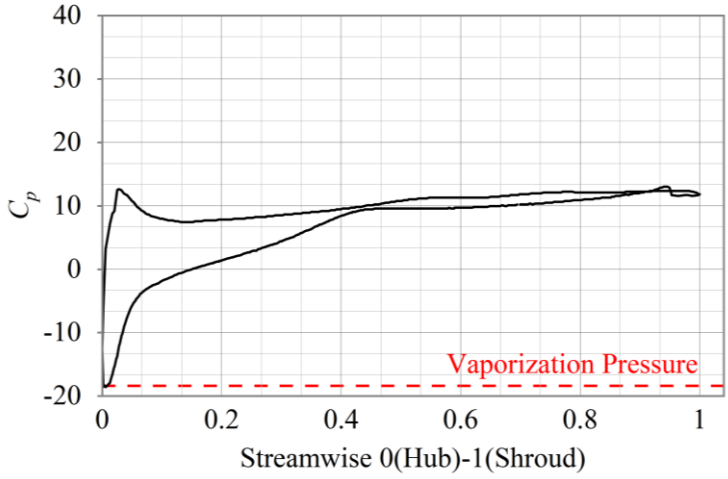

(g) σ =0.412 the inducer blade

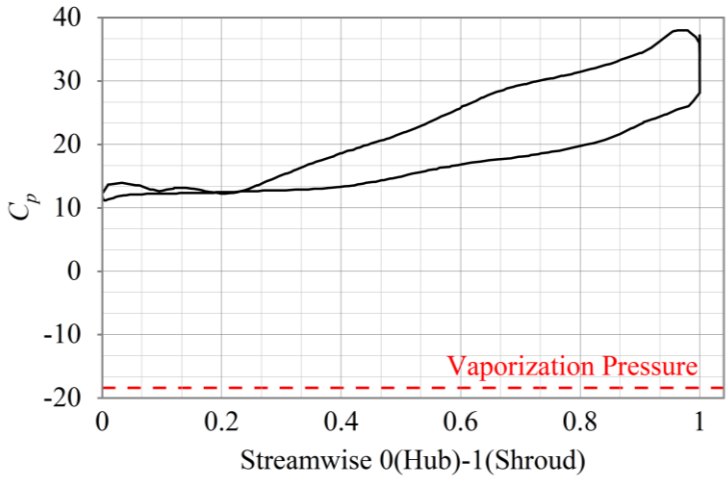

(h) σ =0.412 the impeller blade

Fig. 18. The pressure load distribution on the blades of the inducer-impeller

Fig. 18 shows the expansion at span 0.9 for the same inducer blade and the impeller blade.

At a cavitation number σ of 0.412, a portion of the suction side of the inducer blade experiences pressure lower than the saturated vapor pressure, resulting in a small area of cavitation, while no cavitation occurs on the impeller blade. As the cavitation number decreases, the surface pressure on both the inducer and impeller blades gradually falls below the saturated vapor pressure, leading to cavitation. Compared to the integrated induced impeller, when cavitation occurs, the envelope area of the pressure distribution curve on the working surface and the back surface of the inducer-impeller is smaller, indicating a more significant decline in working performance.

6. Discussions

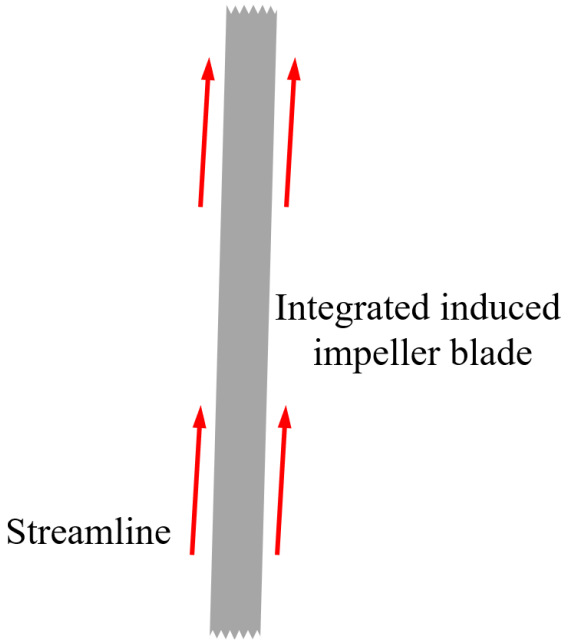

Figure 19. Streamline of the integrated induced impeller

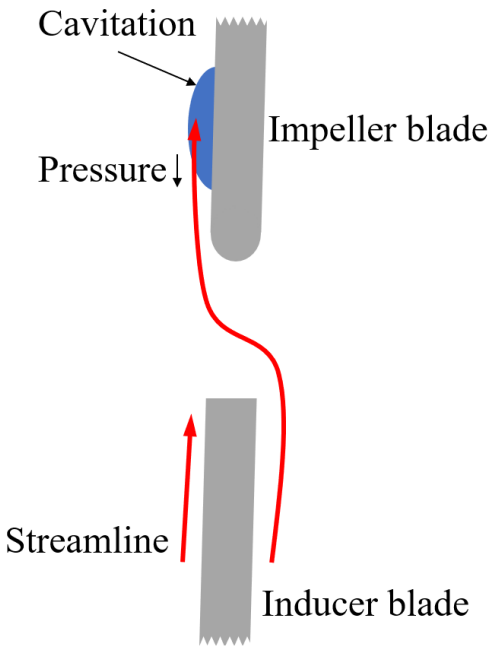

Figure 20. Streamline of the inducer-impeller in the first scenario

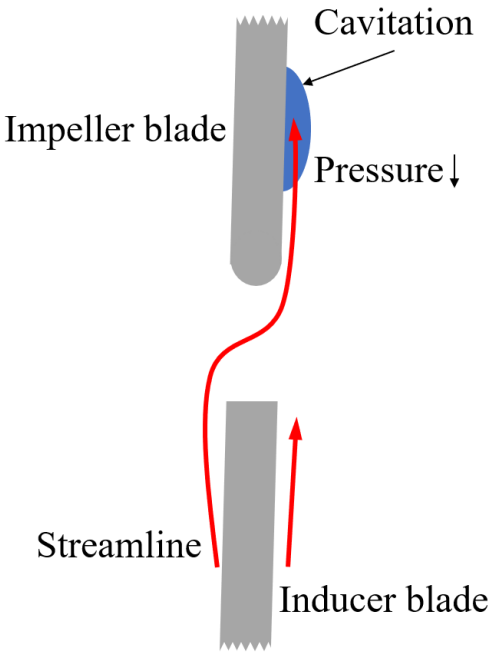

Figure 21. Streamline of the inducer-impeller in the second scenario

Fig. 19 displays a type of streamline pattern in the integrated induced impeller, where the fluid in the integrated induced impeller basically flows along the shape of the blades. Fig. 20 and Fig. 21 show two types of streamline patterns in the inducer-impeller, where there is a gap between the inducer and the impeller. In these two scenarios, the fluid may experience flow separation during its movement. The occurrence of flow separation can cause a reduction in pressure on one side of the blade, leading to a pressure difference between the two sides of the blade, and subsequently causing cavitation.

7. Conclusions

(1) Compared to the inducer-impeller, the integrated induced impeller is more difficult to manufacture, the difficulty of replacing the impeller is increased, and the cost is higher. The head of the integrated induced impeller is inferior to that of the inducer-impeller, but its efficiency is superior to that of the inducer-impeller.

(2) Overall, the cavitation resistance performance of the integrated induced impeller is significantly better than that of the inducer-impeller. The cavitation number at which the integrated induced impeller experiences critical cavitation is noticeably lower than that of the inducer-impeller. When cavitation occurs, the efficiency of the integrated induced impeller is higher than the efficiency of the inducer-impeller.

(3) Combined with the vapor volume distribution diagram, it can be seen that the cavities within the impeller connect and block the flow channel, which is one of the reasons for the decline in impeller efficiency. Looking at the pressure load distribution on the blade surface, the reduction in the area enclosed by the pressure side and suction side load distribution curves indicates a decrease in the impeller's head increase value, further leading to a decline in cavitation and impeller efficiency.

Funding

This study is supported by the National Natural Science Foundation of China, Grant No. 52079142.

Conflict of Interest

The authors declare that they have no conflict of interest.

Author Contributions

Conceptualization, Ruofu Xiao. and Ran Tao.; validation, Xingyu Fang., Tengjiao Guo., Kun Lin; formal analysis, Xingyu Fang.; investigation, Yanzhao Wu.; resources, Ruofu Xiao.; data curation, Tengjiao Guo.; writing—original draft preparation, Xingyu Fang.; writing—review and editing, Ran Tao.; visualization, Xingyu Fang.; supervision, Ran Tao.; project administration, Ran Tao.; funding acquisition, Ruofu Xiao. All authors have read and agreed to the published version of

the manuscript.

Data Availability

Data available on request from the corresponding author.

Ethical approval and Consent to participate

This article does not contain any studies with human participants or animals performed by any of the authors. Informed consent was obtained from all individual participants included in the study.

Acknowledgements

The author gratefully acknowledges the contributions of all co-authors and the financial support received from the National Natural Science Foundation of China.

References

1. Dong L, Shang H, Zhao Y, et al. Study on unstable characteristics of centrifugal pump under different cavitation stages[J]. Journal of Thermal Science, 2019, 28: 608-620.
2. Wang C, Huang B, Wang G, et al. Unsteady pressure fluctuation characteristics in the process of breakup and shedding of sheet/cloud cavitation[J]. International Journal of Heat and Mass Transfer, 2017, 114: 769-78 5.
3. Kimura T, Yoshida Y, Hashimoto T, et al. Numerical simulation for vortex structure in a turbopump inducer: Close relationship with appearance of cavitation instabilities[J]. 2008.
4. Wade R B. Linearized theory of a partially cavitating cascade of flat plate hydrofoils[J]. Applied Scientific Research, 1967, 17: 169-18 8.
5. Huang D, Zhuang Y, Cai R. A computational method for cavitational flows based on energy conservation[J]. Proceedings of the Institution of Mechanical Engineers, Part C: Journal of Mechanical Engineering Science, 2007, 221(11): 1333-1338.
6. Lichao W E I, Wenwu S, Jianwei S H I. Numerical simulation and analysis of the flow at the inlet of a high speed centrifugal pump based on the software CFD[J]. Journal of Engineering for Thermal Energy and Power, 2016, 31(7): 103-109.
7. Binama M, Muhirwa A, Bisengimana E. Cavitation effects in centrifugal pumps-A review[J]. International Journal of Engineering Research and Applications, 2016, 6(5): 52-63.
8. Tan L, Zhu B, Wang Y, et al. Numerical study on characteristics of unsteady flow in a centrifugal pump volute at partial load condition[J]. Engineering computations, 2015, 32(6): 1549-1566.
9. Athavale M M, Li H Y, Jiang Y U, et al. Application of the full cavitation model to pumps and inducers[J]. International Journal of Rotating Machinery, 2002, 8(1): 45-56.
10. Li J, Liu L J, Li G J. Numerical study on the effect of cavitation number on the hydraulic performance of centrifugal pumps[J]. Journal of engineering thermophysics, 2010, 31(5): 77 3-776.
11. Lu J, Yuan S, Luo Y, et al. Numerical and experimental investigation on the development of cavitation in a centrifugal pump[J]. Proceedings of the Institution of Mechanical Engineers, Part E: Journal of Process Mechanical Engineering, 2016, 230(3): 171-182.
12. Li C Y, Ceccio S L. Interaction of single travelling bubbles with the boundary layer and attached cavitation[J]. Journal of Fluid Mechanics, 1996, 322: 329-353.
13. Arakeri V H, Acosta A J. Viscous effects in the inception of cavitation on axisymmetric bodies[J]. 1973.
14. Chudina M. Noise as an indicator of cavitation in a centrifugal pump[J]. Acoustical physics, 2003, 49(4): 463-474.
15. Zhu D, Tao R, Xiao R. Anti-cavitation design of the symmetric leading-edge shape of mixed-flow pump impeller blades[J]. Symmetry, 2019, 11(1): 46.
16. Yang W, Xiao R, Wang F, et al. Influence of splitter blades on the cavitation performance of a double suction centrifugal pump[J]. Advances in Mechanical Engineering, 2014, 6:963197.
17. Zhang F, Tao R, Zhu D, et al. Anti-cavitation leading-edge profile design of centrifugal pump impeller blade based on genetic algorithm and decision tree[J]. Journal of the Brazilian Society of Mechanical Sciences and Engineering, 2022, 44(7): 279.
18. Pouffary B, Patella R F, Reboud J L, et al. Numerical simulation of 3D cavitating flows: analysis of cavitation head drop in turbomachinery[J]. 2008.

19. Guo X M, Zhu Z C, Cui B L, et al. Anti-cavitation performance of a splitter-bladed inducer under different flow rates and different inlet pressures[J]. Science China Technological Sciences, 2015, 58: 2131-2138.
20. Guo X, Zhu Z, Shi G, et al. Effects of rotational speeds on the performance of a centrifugal pump with a variable-pitch inducer[J]. Journal of hydrodynamics, 2017, 29(5): 854-862.
21. Zhang H, Xia B, Kong F, et al. Experimental investigation of cavitation characteristics for a high-speed inducer with a great flow rate[J]. Advances in Mechanical Engineering, 2022, 14(3): 16878132221087510.
22. Ma L L, Wang C, Chen Y, et al. The Study of Using the Inducer to Improve the Cavitation Performance of a Centrifugal Pump[C] // Journal of Physics: Conference Series. IOP Publishing, 2024, 2752(1): 0121 22.
23. Sun-Sheng Y, Fan-Yu K, Jian-Hui F, et al. Numerical research on effects of splitter blades to the influence of pump as turbine[J]. International Journal of Rotating Machinery, 2012, 2012(1): 123093.
24. Kergourlay G, Younsi M, Bakir F, et al. Influence of splitter blades on the flow field of a centrifugal pump: test-analysis comparison [J]. International Journal of Rotating Machinery, 2007, 2007(1): 085024.
25. Chabannes L, Štefan D, Rudolf P. Effect of splitter blades on performances of a very low specific speed pump[J]. Energies, 2021, 14 (13): 3785.
26. Korkmaz E, Gölcü M, Kurbanoğlu C. Effects of blade discharge angle, blade number and splitter blade length on deep well pump performance[J]. Journal of Applied Fluid Mechanics, 2017, 10(2): 529-540.
27. Siddique M H, Samad A, Hossain S. Centrifugal pump performance enhancement: Effect of splitter blade and optimization[J]. Proceedings of the Institution of Mechanical Engineers, Part A: Journal of Power and Energy, 2022, 236(2): 391-402.
28. Zeng G, Li Q, Wu P, et al. Investigation of the impact of splitter blades on a low specific speed pump for fluid-induced vibration[J]. Journal of Mechanical Science and Technology, 2020, 34: 2883-2893.